


# Evidence of a finite-time pointlike singularity solution for the Euler equations for perfect fluids

Diego Martínez-Argüello  and Sergio Rica 

*Instituto de Física, Pontificia Universidad Católica de Chile, Avenida Vicuña Mackenna 4860, Santiago, Chile*



(Received 27 April 2024; accepted 20 August 2024; published 5 September 2024)

This paper investigates the evolution of the Euler equations near a potential blow-up solution. We employ an approach where this solution exhibits second-type self-similarity, characterized by an undetermined exponent  $\nu$ . This exponent can be seen as a nonlinear eigenvalue, determined by the solution of a self-similar partial differential equation with appropriate boundary conditions. Specifically, we demonstrate the existence of an axisymmetric solution of the Euler equations by expanding the axial vorticity using associated Legendre polynomials as a basis. This expansion results in an infinite hierarchy of ordinary differential equations, which, when truncated up to a certain order  $N^*$ , allows for the numerical resolution of a finite set of ordinary differential equations. Through this numerical analysis, we obtain a solution that satisfies the appropriate boundary conditions for a specific value of the exponent  $\nu$ . By exploring various truncations, we establish a sequence in  $N^*$  for the parameter  $\nu_{N^*}$ , providing evidence of the convergence of the exponent  $\nu$ . Our findings suggest a self-similar exponent  $\nu \approx 2$ , presenting a promising path for a numerical or analytical approach indicating that  $\nu$  may indeed be exactly 2.

DOI: [10.1103/PhysRevFluids.9.094401](https://doi.org/10.1103/PhysRevFluids.9.094401)

## I. INTRODUCTION

The Euler equations for an inviscid and incompressible fluid aimed of motion with velocity  $\mathbf{v}(\mathbf{x}, t)$  are as follows:

$$\frac{\partial}{\partial t} \mathbf{v} + \mathbf{v} \cdot \nabla \mathbf{v} = -\nabla p, \quad (1)$$

$$\nabla \cdot \mathbf{v} = 0, \quad (2)$$

where the scalar field  $p(\mathbf{x}, t)$  stands for the pressure, that takes into account the internal forces acting on a fluid element. From a taxonomic point of view, Euler equations are a set of nonlinear and nonlocal partial differential equations. The nonlocality comes precisely from the pressure term,  $p(\mathbf{x}, t)$ , which, after taking the divergence of Eq. (1), follows as a solution to a Poisson equation.

Among other conserved quantities [1], the Euler equations preserve kinetic energy:

$$\frac{d}{dt} \int |\mathbf{v}(\mathbf{x}, t)|^2 d\mathbf{x} = 0. \quad (3)$$

The Euler equations (1) and (2), along with the conservation law (3), necessitate smoothness of the velocity field and its derivatives, as well as appropriate boundary conditions at infinity. In an unbounded domain, we require the velocity field to diminish at infinity in such a way that  $\lim_{r \rightarrow \infty} |\mathbf{v}|^2 r^3 \rightarrow 0$ , ensuring that the flow maintains finite energy. Besides the equations and boundary conditions, the initial condition must be divergence-free and smooth or infinitely differentiable:  $\mathbf{v}(\mathbf{x}, t = 0) = \mathbf{v}_0(\mathbf{x})$ , with  $\nabla \cdot \mathbf{v}_0 = 0$ .

Equations (1) and (2), written by Euler in 1757 [2], constitute the second partial differential equation (PDE) ever recorded in history. Unlike other PDEs in physics, the Euler equations have

yet to reveal all their secrets. Particularly, the regularity problem persists: For a given smooth initial condition for the velocity field with finite energy, does the velocity field remain regular for all times, or does a smooth initial velocity blow-up in finite time? This question has intrigued physicists and mathematicians for about a century, since Lichtenstein and Gunter [3,4].

The hundred years of searching for finite-time singularities as solutions of the Euler equations have seen significant progress in recent years. Numerical simulations by Luo and Hou [5] suggested the possible existence of a finite-time singularity in the axisymmetric Euler equations near the wall boundary. This finite-time singularity has been numerically verified by a completely different approach, in Ref. [6], using physics-informed neural networks applied to the 2D Boussinesq equations, which in the singularity limit are equivalent to the Euler axisymmetric equations. Last, Chen and Hou advanced a formal mathematical proof of the existence of such a singularity [7].

However, Luo and Hou observed that the singularity arises on a rim at the boundary of a finite radius domain, indicating that boundary conditions play a major role. Conversely, the idea of the existence of a pointlike singularity has been circulating over the years [8,9], in particular in connection with the anomalous dissipation in fully developed turbulence [10–13]. An explicit approximation for an axisymmetric flow was proposed by Elgindi [14] recently; however, this singularity sets up as a consequence of a nonsmooth initial condition. The question of a pointlike finite-time singularity as a consequence of the evolution by Euler equations in an infinite domain for a smooth and finite energy initial condition remains open. In this article, we focus on the search for such a singularity in three-dimensional space.

We provide evidence for the existence of a self-similar blow-up solution to the axisymmetric version of the Euler equations for an incompressible and inviscid fluid. By assuming a second type of self-similarity with an unknown exponent,  $\nu$ , we solve the Euler equations in an axisymmetric configuration using spherical coordinates and by expanding the axial vorticity in a basis of associated Legendre polynomials. This transforms the original problem into an infinite set of ordinary differential equations (ODEs) governing the amplitudes of the final axial vorticity and the swirl velocity. By truncating this set of ODEs up to a certain order  $N^*$ , the system is ultimately solved numerically, suggesting a convergent scenario for the solutions and the nonlinear eigenvalue,  $\nu$ .

## II. LERAY'S SELF-SIMILAR SOLUTION

In the following, instead of searching for an arbitrary singularity, we focus on a special kind of self-similar singularity that has been the center of research in the past 25 years [15]. Following Leray [16], Pomeau [8–11] suggested a pointlike singularity solution of the equations of fluid dynamics (1) and (2) in the form

$$\mathbf{v}(\mathbf{x}, t) = \frac{1}{(t_c - t)^{1-\nu}} \mathbf{V}\left(\frac{\mathbf{x}}{(t_c - t)^\nu}\right), \quad (4)$$

$$p(\mathbf{x}, t) = \frac{1}{(t_c - t)^{2(1-\nu)}} \mathcal{P}\left(\frac{\mathbf{x}}{(t_c - t)^\nu}\right). \quad (5)$$

Here,  $\mathbf{V}(\boldsymbol{\xi})$  and  $\mathcal{P}(\boldsymbol{\xi})$  are the self-similar velocity profile and pressure, respectively, and  $\boldsymbol{\xi} = \mathbf{x}/(t_c - t)^\nu$  is a self-similar 3D space coordinate. The self-similar or Euler-Leray equations read [8]:

$$(1 - \nu)\mathbf{V}(\boldsymbol{\xi}) + \nu(\boldsymbol{\xi} \cdot \nabla_{\boldsymbol{\xi}})\mathbf{V} + (\mathbf{V} \cdot \nabla_{\boldsymbol{\xi}})\mathbf{V} = -\nabla_{\boldsymbol{\xi}}\mathcal{P}, \quad (6)$$

$$\nabla_{\boldsymbol{\xi}} \cdot \mathbf{V} = 0. \quad (7)$$

As discussed in Eggers and Fontelos [15] for any  $\mathbf{x} \neq \mathbf{0}$ , if the self-similar solutions are stable, and thus related to the finite-time singularity of the original Euler equations, then it is expected that near the singularity the velocity profile becomes stationary as  $t \rightarrow t_c$ , because the self-similar *ansatz* is

asymptotic for  $t_c$  fixed and finite [17]. Therefore, the boundary conditions must be

$$((1 - \nu) + \nu \boldsymbol{\xi} \cdot \nabla_{\boldsymbol{\xi}}) \mathbf{V}(\boldsymbol{\xi}) \rightarrow 0 \quad \text{as} \quad |\boldsymbol{\xi}| \rightarrow \infty. \quad (8)$$

Moreover, the self-similar velocity  $\mathbf{V}(\boldsymbol{\xi})$  is infinitely differentiable at  $|\boldsymbol{\xi}| \rightarrow 0$ .

Because of conserved quantities, the Leray type of self-similar solution imposes restrictions on the value of  $\nu$ . The energy of a pointlike singularity must not diverge as  $t \rightarrow t_c$ , thus

$$\mathcal{E} = \frac{1}{2} \int \mathbf{v}^2 d^3 \mathbf{x} = \frac{1}{2} (t_c - t)^{2(\nu-1)} \int \left| \mathbf{V} \left( \frac{\mathbf{x}}{(t_c - t)^\nu} \right) \right|^2 d^3 \mathbf{x} = \frac{1}{2} (t_c - t)^{5\nu-2} \int |\mathbf{V}(\boldsymbol{\xi})|^2 d^3 \boldsymbol{\xi} \quad (9)$$

imposes  $\nu \geq 2/5$  as  $t \rightarrow t_c$  [18]. We emphasize the fact that the integral in the self-similar variable,  $\int |\mathbf{V}(\boldsymbol{\xi})|^2 d^3 \boldsymbol{\xi}$ , diverges accordingly with the boundary condition (8). Contrary to Schonbek's [19], who imposes  $\nu < 3/5$ , values for  $\nu \geq 3/5$  cannot be ruled out, as the asymptotic behavior described by Eq. (8) is only the inner asymptotic limit as  $t \rightarrow t_c$ . This phenomena has been already noticed in different self-similarities as it is the case of the Nonlinear Schrödinger equation (see [12] for details and references).

Equivalent to the Euler equations (1) is the equation for the vorticity field:

$$\boldsymbol{\omega} = \nabla \times \mathbf{v}. \quad (10)$$

The pressure is eliminated, and the dynamics of the vorticity reads

$$\partial_t \boldsymbol{\omega} + \nabla \times (\boldsymbol{\omega} \times \mathbf{v}) = 0. \quad (11)$$

Similarly, the Helmholtz equation (11) is also a nonlinear and nonlocal partial differential equation: the velocity in Eq. (11) is a nonlocal functional of vorticity (10), as follows from the Biot-Savart law.

As a consequence of the vorticity (10), the self-similar vorticity reads

$$\boldsymbol{\omega}(\mathbf{x}, t) = \frac{1}{(t_c - t)} \boldsymbol{\Omega} \left( \frac{\mathbf{x}}{(t_c - t)^\nu} \right). \quad (12)$$

The singular dependence  $1/(t_c - t)$ , comes essentially by a dimensional analysis, more important, it does not depend on the exponent  $\nu$ , thus, the Beale-Kato-Magda theorem [20] does not contradict the singular character of the solution. The self-similar vorticity equation satisfies

$$\boldsymbol{\Omega} + \nu \boldsymbol{\xi} \cdot \nabla_{\boldsymbol{\xi}} \boldsymbol{\Omega} + \nabla_{\boldsymbol{\xi}} \times (\boldsymbol{\Omega} \times \mathbf{V}) = 0, \quad (13)$$

together with

$$\boldsymbol{\Omega} = \nabla_{\boldsymbol{\xi}} \times \mathbf{V}, \quad \& \quad \nabla_{\boldsymbol{\xi}} \cdot \mathbf{V} = 0,$$

and the boundary condition

$$(1 + \nu \boldsymbol{\xi} \cdot \nabla_{\boldsymbol{\xi}}) \boldsymbol{\Omega}(\boldsymbol{\xi}) \rightarrow 0 \quad \text{as} \quad |\boldsymbol{\xi}| \rightarrow \infty, \quad (14)$$

and  $\boldsymbol{\Omega}(\boldsymbol{\xi})$  is smooth at  $\boldsymbol{\xi} \rightarrow \mathbf{0}$ .

The main findings of this paper pertain to the solutions of the self-similar Euler-Leray equations in the forms given by Eqs. (6) and (7), as well as the equivalent Helmholtz-Leray equation (13), subject to appropriate boundary conditions. These equations are solved in an axisymmetric configuration using spherical coordinates, and by expanding the relevant fields (axial vorticity, swirl velocity, and stream function) in a base of Legendre polynomials. The solutions lead to a self-similar exponent of  $\nu \approx 2.03$ , and the corresponding self-similar field patterns are illustrated in Fig. 1.

In the case of Luo and Hou [5], the singular solutions (4), (5), and (12) are different. First, the singularity arises at a rim and not at a point, as in the case presented here. The specific self-similar

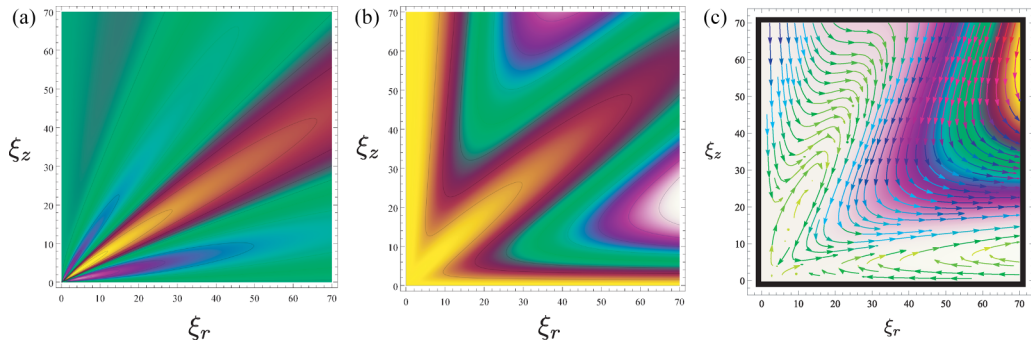


FIG. 1. Patterns of the self-similar flows in the plane ( $\xi_r = \xi \sin \theta$ ,  $\xi_z = \xi \cos \theta$ ), for  $N^* = 4$ . The plots include (a)  $\Omega_\phi(\xi_r, \xi_z)$ , (b)  $V_\phi^2(\xi_r, \xi_z)$ , and (c)  $\Psi(\xi_r, \xi_z)$ , and the flow lines represents the velocity field  $(V_{\xi_r}, V_{\xi_z})$ .

ansatz of Luo and Hou is of the form

$$v_\phi(r, z, t) = (t_c - t)^{\gamma_u} U\left(\frac{R - r}{(t_c - t)^{\gamma_l}}, \frac{z}{(t_c - t)^{\gamma_\omega}}\right),$$

$$\omega_\phi(r, z, t) = (t_c - t)^{\gamma_\omega} \Omega\left(\frac{R - r}{(t_c - t)^{\gamma_l}}, \frac{z}{(t_c - t)^{\gamma_\omega}}\right),$$

and they numerically obtained the following exponents:

$$\gamma_l \approx 2.91, \quad \gamma_u \approx 0.46, \quad \gamma_\omega \approx -1.$$

In the ansatz,  $R$  represents the radius of the cylindrical domain, set to unity in Ref. [5]. The exponent  $\gamma_l$ , in Luo and Hou's original notations, is analog to our current exponent  $\nu$ . We underline, that the problem of a pointlike singularity discussed here, is intrinsically different, from the one of a rimlike singularity considered previously by Luo and Hou [5].

### III. AXISYMMETRIC SELF-SIMILAR FLOW WITH SWIRL IN SPHERICAL COORDINATES

Special attention is devoted to axisymmetric flows because they are simpler than the general case [5–7, 14, 21]. The axisymmetric geometry is typically described in cylindrical coordinates; however, in this context, we employ spherical coordinates ( $\xi = |\mathbf{x}|/(t_c - t)^\nu$ ,  $\theta$ ,  $\phi$ ), where the self-similar velocity flow,  $\mathbf{V} = V_\xi \hat{\xi} + V_\phi \hat{\phi} + V_\theta \hat{\theta}$ , the vorticity  $\boldsymbol{\Omega} = \nabla_\xi \times \mathbf{V}$ , and the pressure  $\mathcal{P}$  do not explicitly depend on the axial angular variable  $\phi$ .

The pressure cancels out in the Euler-Leray equation (6) for the axial (or swirl) velocity  $V_\phi$  leading to

$$(1 - \nu)V_\phi + (\nu\xi + V_\xi)\frac{\partial V_\phi}{\partial \xi} + \frac{V_\theta}{\xi}\frac{\partial V_\phi}{\partial \theta} + \frac{(V_\xi + \cot \theta V_\theta)}{\xi}V_\phi = 0. \quad (15)$$

By using the following characteristics:  $\frac{d\xi}{ds} = (\nu\xi + V_\xi)$  and  $\frac{d\theta}{ds} = \frac{V_\theta}{\xi}$ , Eq. (15) transforms into

$$\frac{d(\xi \sin \theta V_\phi)}{ds} = (2\nu - 1)(\xi \sin \theta V_\phi).$$

Remarkably, if  $\nu > 1/2$ , and if  $\xi \sin \theta V_\phi \geq 0$  on a boundary of the domain, then  $\xi \sin \theta V_\phi$  is nonnegative along the characteristics. In the following, we restrict ourselves to the situation of a non negative swirl velocity ( $V_\phi > 0$  for  $0 < \theta < \pi/2$ ) with an odd flow:  $V_\phi(\xi, \theta) = -V_\phi(\xi, \pi - \theta)$ .

In this particular scenario, it follows from Eq. (15) that

$$2(1 - \nu)V_\phi^2 + (\nu\xi + V_\xi)\frac{\partial V_\phi^2}{\partial \xi} + \frac{V_\theta}{\xi}\frac{\partial V_\phi^2}{\partial \theta} = -2\frac{(V_\xi + \cot \theta V_\theta)}{\xi}V_\phi^2. \quad (16)$$

So far,  $V_\xi$  and  $V_\theta$  have not been determined yet. The incompressibility condition (7) introduces naturally a stream function,  $\Psi$ :

$$V_\xi = \frac{1}{\xi^2 \sin \theta} \frac{\partial \Psi}{\partial \theta}, \quad V_\theta = -\frac{1}{\xi \sin \theta} \frac{\partial \Psi}{\partial \xi}, \quad (17)$$

such that the velocity flow remains incompressible. Finally, instead of writing equations for the components  $V_\xi$  and  $V_\theta$ , an equation for the axial component of vorticity in spherical coordinates is considered:

$$\Omega_\phi = \frac{1}{\xi} \left( \frac{\partial(\xi V_\theta)}{\partial \xi} - \frac{\partial V_\xi}{\partial \theta} \right). \quad (18)$$

It is easy to see that the vorticity field,  $\Omega_\phi(\xi, \theta)$ , and the stream function,  $\Psi(\xi, \theta)$ , possess the same symmetry as the swirl velocity, *i.e.*  $\Omega_\phi(\xi, \theta) = -\Omega_\phi(\xi, \pi - \theta)$  and  $\Psi(\xi, \theta) = -\Psi(\xi, \pi - \theta)$ . Therefore, we confine our analysis to the quadrant  $0 \leq \xi < \infty$  and  $0 \leq \theta \leq \pi/2$ .

The equation for  $\Omega_\phi$  is derived after Eq. (13):

$$\Omega_\phi + (\nu\xi + V_\xi)\frac{\partial \Omega_\phi}{\partial \xi} + \frac{V_\theta}{\xi}\frac{\partial \Omega_\phi}{\partial \theta} = \frac{(V_\xi + \cot \theta V_\theta)}{\xi}\Omega_\phi + \frac{1}{\xi} \left( \cot \theta \frac{\partial V_\phi^2}{\partial \xi} - \frac{1}{\xi} \frac{\partial V_\phi^2}{\partial \theta} \right). \quad (19)$$

Finally, the stream function,  $\Psi$ , is related to axial vorticity component by

$$\frac{\partial^2 \Psi}{\partial \xi^2} + \frac{1}{\xi^2} \left( \frac{\partial^2 \Psi}{\partial \theta^2} - \cot \theta \frac{\partial \Psi}{\partial \theta} \right) = -\xi \sin \theta \Omega_\phi(\xi, \theta). \quad (20)$$

Equations (16), (17), (19), and (20) form a self-contained coupled partial differential system for the axisymmetric perfect fluid. An interesting aspect of this system is that it is “linear” in  $\Omega_\phi$  and  $V_\phi^2$ . The nonlinearities come from  $\Psi = \Psi[\Omega_\phi]$  via  $V_\xi$  and  $V_\theta$  in Eq. (17).

The boundary conditions for the relevant fields are such that at  $\theta = 0$ :

$$\Omega_\phi(\xi, \theta = 0) = V_\phi^2(\xi, \theta = 0) = \Psi(\xi, \theta = 0) = 0, \quad (21)$$

to ensure regularity at the axis, and, because of the odd symmetry regarding the plane ( $\theta = \pi/2$ ):

$$\Omega_\phi(\xi, \theta = \pi/2) = V_\phi^2(\xi, \theta = \pi/2) = \Psi(\xi, \theta = \pi/2) = 0, \quad (22)$$

while

$$\Omega_\phi + \nu\xi \frac{\partial \Omega_\phi}{\partial \xi} \rightarrow 0 \quad \text{and} \quad 2(1 - \nu)V_\phi^2 + \nu\xi \frac{\partial V_\phi^2}{\partial \xi} \rightarrow 0, \quad (23)$$

as  $\xi \rightarrow \infty$  and  $0 \leq \theta \leq \pi/2$ .

Last, at the origin,  $\xi = 0$ , it is imposed that all variables are smooth; *i.e.*, the fields are developable in a Taylor expansion near  $\xi = 0$ .

#### IV. ASYMPTOTIC EXPANSION USING ASSOCIATED LEGENDRE POLYNOMIALS

Equations (16), (17), (19), and (20) along with the boundary conditions (21), (22), and (23), and the regularity condition at the origin, are solved as follows. First, all functions of interest are expanded in associated Legendre polynomials:

$$\Omega_\phi(\xi, \theta) = \sum_{n=1}^{\infty} F_n(\xi)y_n(\theta), \quad V_\phi^2(\xi, \theta) = \xi^2 \sum_{n=1}^{\infty} G_n(\xi)y_n(\theta), \quad \Psi(\xi, \theta) = \sum_{n=1}^{\infty} \Psi_n(\xi)y_n(\theta). \quad (24)$$

Here, the  $\xi^2$  prefactor for  $V_\phi^2$  is for convenience. In these expansions, the functions  $y_n(\theta) = -c_n \sin \theta P_{2n}^1(\cos \theta)$  are related to the associated Legendre polynomials. The  $y_n(\theta)$ 's satisfy the boundary conditions because  $y_n(0) = y_n(\pi/2) = 0$ . Moreover, with the adequate value of  $c_n$  the set  $y_n$  is orthonormal and diagonalizes the elliptic operator in the left-hand side of Eq. (20). The explicit dependence of  $c_n$  is given in Eq. (A3) in Appendix A.

The amplitudes  $F_n(\xi)$  and  $G_n(\xi)$  satisfy the boundary conditions, that follows from Eq. (23):

$$F_n(\xi) + \nu \xi F_n'(\xi) \rightarrow 0 \quad \text{and} \quad 2G_n(\xi) + \nu \xi G_n'(\xi) \rightarrow 0, \quad (25)$$

as  $\xi \rightarrow \infty$ . In the addition, the amplitudes  $F_n(\xi)$  and  $G_n(\xi)$  are differentiable at  $\xi = 0$ .

By substituting Eq. (24) into Eq. (20), we obtain using the standard method of Green functions (See Appendix A):

$$\Psi(\xi, \theta) = \xi^3 \sum_{n=1}^{\infty} (N_n(\xi) + L_n(\xi)) y_n(\theta), \quad (26)$$

with

$$N_n(\xi) = \xi^{-2n-3} \sum_{m=1}^{\infty} \beta_{nm} \int_0^\xi F_m(u) u^{2n+2} du \quad \text{and} \quad L_n(\xi) = \xi^{2n-2} \sum_{m=1}^{\infty} \beta_{nm} \int_\xi^\infty F_m(u) u^{-2n+1} du. \quad (27)$$

Here,  $\beta_{nm}$  are pure numbers that arise from the inner product in the projection process (see Eq. (A8) in Appendix A). The function  $L_1(\xi)$  corresponds exactly to the approximation used by Elgindi [14], who neglected other radial components such as  $N_n(\xi)$  and  $L_n(\xi)$  with  $n > 1$  near the singularity's origin. Although all these functions appear to be negligible, the function  $N_1(\xi)$  appears to be relevant for numerical computations. Nevertheless, in the analytics, we retain all amplitudes for the sake of generality.

Finally, by replacing  $\Omega_\phi$  and  $V_\phi^2$  into Eqs. (16) and (19), and projecting into the basis  $y_n(\theta)$  it is shown that the amplitudes  $F_n(\xi)$  and  $G_n(\xi)$  satisfy an infinite coupled set of ordinary differential equations, constituting an autonomous dynamical system with  $s = \log \xi$  as the variable (see Appendix B for the derivation). This dynamical system can be formally expressed as

$$\begin{aligned} F_n'(s) &= \mathcal{U}_F(\{F_n\}, \{G_n\}, \{N_n\}, \{L_n\}, \nu), \\ G_n'(s) &= \mathcal{U}_G(\{G_n\}, \{N_n\}, \{L_n\}, \nu), \\ N_n'(s) &= -(2n+3)N_n + \sum_m \beta_{nm} F_m, \\ L_n'(s) &= 2(n-1)L_n - \sum_m \beta_{nm} F_m. \end{aligned} \quad (28)$$

The functionals  $\mathcal{U}_F(\cdot)$  and  $\mathcal{U}_G(\cdot)$  (the last one is independent of the amplitudes  $\{F_n\}$ 's) are formally linear in the amplitudes  $F_n$  and  $G_n$ . As already said, nonlinearities arise from the couplings with  $N_n$  and  $L_n$ . As these equations result from the projection of the original PDE, various matrix elements, such as  $\beta_{nm}$ , appear as pure numbers. The only unknown parameter involved in the dynamical system is  $\nu$ , which is a kind of nonlinear eigenvalue, and must be determined by the solution of the ODE system and the right boundary conditions. The full set of equations is explicitly written in Appendix B.

## V. NONLINEAR EIGENVALUE SOLUTION VIA A DYNAMICAL SYSTEM APPROACH

It follows that the solution to the original problem is mapped into the search for a heteroclinic orbit of the dynamical system (28). This heteroclinic orbit connects two distinct fixed points corresponding to the boundary conditions of the original problem (see Ref. [15] for generalities). In

the current case, the fixed points of the dynamical system (28) correspond to the boundary conditions (21), (22) ( $s \rightarrow -\infty$ ), and (23) ( $s \rightarrow \infty$ ) for the axisymmetric Euler-Leray equations and are as follows:

$$\text{FP1} : F_n = G_n = N_n = L_n = 0, \quad s \rightarrow \infty, \quad (29)$$

$$\text{FP2} : L_1 = L_1^{(0)} \neq 0, \quad F_n = G_n = N_n = L_{n>1} = 0, \quad s \rightarrow -\infty. \quad (30)$$

The heteroclinic orbit starts at FP2 as  $s \rightarrow -\infty$ , following a precise unstable manifold, and should reach the stable manifold of the other fixed point FP1 as  $s \rightarrow \infty$ . To determine such a trajectory, one must study the local stability near both fixed points.

The behavior around FP1 arises from the stationary condition of the asymptotic self-similarity as  $t \rightarrow t_c$  and is determined by Eq. (25):

$$\begin{aligned} F_n &= F_n^{(\infty)} e^{-s/\nu}, \quad G_n = G_n^{(\infty)} e^{-2s/\nu}, \\ N_n &= N_n^{(\infty)} e^{-(2n+3)s} + \frac{\Lambda_n}{2n+3-1/\nu} e^{-s/\nu}, \\ L_n &= L_n^{(\infty)} e^{2(n-1)s} + \frac{\Lambda_n}{2n-2+1/\nu} e^{-s/\nu}, \quad \text{as } s \rightarrow \infty. \end{aligned} \quad (31)$$

Here

$$\Lambda_n = \sum_{m=1}^{\infty} \beta_{nm} F_m^{(\infty)}.$$

The constants  $F_n^{(\infty)}$  and  $G_n^{(\infty)}$  cannot be determined through the asymptotic analysis. The coefficients  $N_n^{(\infty)}$  and  $L_n^{(\infty)}$  are found to vanish (i.e.,  $N_n^{(\infty)} = L_n^{(\infty)} = 0$ ), as demonstrated by the integral expressions in Eq. (27). However, the linear behavior of  $L_n(s)$  in Eq. (28) suggests that FP1 is an unstable fixed point. Consequently, the matching conditions strictly enforce that  $L_n^{(\infty)} = 0$  for all  $n \geq 1$ , ensuring FP1 avoids the unstable manifold.

The local analysis of the other fixed point, FP2, is characterized also by an unstable behavior:

$$G_n(s) = \delta g_n e^{\sigma s}, \quad F_n(s) = \delta f_n e^{\sigma s}, \quad L_n(s) = L_1^{(0)} \delta_{n,1} + \delta L_n e^{\sigma s}, \quad N_n(s) = \delta N_n e^{\sigma s}, \quad s \rightarrow -\infty. \quad (32)$$

The fixed point FP2 corresponds to the boundary condition where axial vorticity, swirl velocity, and stream function must vanish as  $\xi \rightarrow 0$ . Therefore, the exponent  $\sigma$  has to be positive, moreover because of the regularity of the solution at the origin,  $\xi = 0$  ( $s \rightarrow -\infty$ ),  $\sigma$  must be an integer, hence  $\sigma \in \{1, 2, 3, \dots\}$ . We provide solutions for  $\sigma = 2$  in Table I in Appendix F. Furthermore, because we use the variable  $V_\phi^2$ , only even powers are suitable. Although solutions with odd values of  $\sigma$  do exist, they make  $V_\phi$  not smooth at the origin. Nevertheless, we provide some solutions for  $\sigma = 3$  in Table II in Appendix F. The coefficients from the unstable behavior (32) can be investigated to first order, at which the only function that survives from all  $L_n(s)$  and  $N_n(s)$  is  $L_1(s)$  through the coupling of  $L_1^{(0)}$  with  $\delta f_n$  and  $\delta g_n$ , and the ODEs (28) are transformed into the algebraic system:

$$[(1 + \nu\sigma)\delta l_p + L_1^{(0)}(a_{l1p} - e_{l1p} + \sigma b_{l1p})]\delta f_p = -[c_{lp} + (2 + \sigma)d_{lp}]\delta g_p, \quad (33)$$

$$[(2 + \nu\sigma)\delta l_p + L_1^{(0)}(a_{l1p} + 2e_{l1p} + (\sigma + 2)b_{l1p})]\delta g_p = 0, \quad (34)$$

$$\delta N_n = \frac{1}{\sigma + 2n + 3} \beta_{nm} \delta f_m, \quad (35)$$

$$\delta L_n = \frac{1}{2n - 2 - \sigma} \beta_{nm} \delta f_m. \quad (36)$$



A nonzero solution of Eq. (34) implies that  $\delta g_n$  is an eigenvector of the matrix

$$(a_{l1p} + 2e_{l1p} + (\sigma + 2)b_{l1p}), \quad (37)$$

with the eigenvalue  $\phi(\sigma) = -(2 + \nu\sigma)/L_1^{(0)}$ . In particular, for a truncation of order  $N^*$  the matrix (37) becomes an  $N^* \times N^*$  square matrix with one real eigenvalue for  $N^*$  odd and two real eigenvalues for  $N^*$  even, from which the unique negative eigenvalue provides a condition such that  $L_1^{(0)} > 0$ . Therefore, we focus on the family of solutions such that  $L_1^{(0)} > 0$ , because solutions such that  $L_1^{(0)} < 0$  are impossible for odd values of  $N^*$ . Consequently, the other amplitudes,  $\delta f_n$ ,  $\delta N_n$ , and  $\delta L_n$ , are fixed only by the right eigenvector  $\delta \bar{g}_n$  and the condition

$$L^{(0)}(\nu, \sigma) = \frac{(2 + \nu\sigma)}{-\phi(\sigma)}, \quad (38)$$

which depends on the self-similar exponent  $\nu$  and the integer index  $\sigma$ .

When integrating the dynamical system in a forward way, FP2 becomes the starting point at  $s \rightarrow -\infty$ , and the integration proceeds forward until reaching  $s \rightarrow \infty$  with the behavior of FP1 (31), following a heteroclinic orbit. Because in the current case, both fixed points are unstable, the tuning of the free parameters becomes delicate. Moreover, we are confronted with an infinite ODE dynamical system. Despite the general arguments outlined earlier, finding an analytical solution is deemed impractical. Therefore, we have opted for a numerical-assisted approach, where the strategy involves truncating the dynamical system up to an order  $N^*$ . In a previous attempt documented in Ref. [21], we pursued such a program. However, due to the use of a Fourier basis instead of the more fitting Legendre basis, a convergent scheme did not fully manifest. We attribute this to the natural suitability of the Legendre basis for this problem, where a convergent scheme is promising.

## VI. NUMERICAL ASSISTED SEARCH OF THE SELF-SIMILAR SOLUTIONS

A numerical approach is used after truncating the angular expansions (24) for a finite value of  $N^*$  to obtain numerical solutions of the truncated hierarchy of ODEs (28) with the boundary conditions (29) and (30). A crucial step in the numerics deals with the selection mechanism of the free parameter,  $\nu$ . This problem is, indeed, a shooting methodology, the parameter  $\nu$  is tuned up to the solution reaches the right boundary condition. To accomplish this task, a *differential evolution* algorithm [22] is implemented. The full differential evolution algorithm is explained in Appendix D.

Differential evolution is basically an optimization algorithm used to find the best value of a set of parameters. In the current case, the algorithm selects  $\nu$  for a given  $\sigma$ , such that the forward integration of the dynamical system reaches the correct asymptotic behavior of the FP1 (29). Besides  $\nu$ , another parameter enters into game because the asymptotic behavior of FP2 (30) is known only up to a constant prefactor. Let be  $\gamma$  this parameter.

This evolutionary algorithm was implemented for  $\sigma = 2$ , that provides the smooth solution of lowest degree at the origin, such that axial vorticity and swirl velocity scale quadratically at the origin:  $\Omega_\phi \sim \xi^2$  and  $V_\phi \sim \xi^2$ . Initially, a set of parameters  $(\nu, \gamma)$  is randomly chosen, then the algorithm searches iteratively for combinations of new sets of parameters which are compared, and the best set is retained. The algorithm is repeated for a number of generations, after which the best pair  $(\nu, \gamma)$  that solves the dynamical system, according to the accomplishment of the asymptotic behavior (31), is selected. The selection of the parameters is done by minimizing the error function:

$$\begin{aligned} \text{Error}[\nu, \gamma] = & \frac{1}{(s_b - s_a)N^*} \sum_{n=1}^{N^*} \int_{s_a}^{s_b} ((F_n(s) + \nu F'_n(s))^2 + (2G_n(s) + \nu G'_n(s))^2 \\ & + (N_n(s) + \nu N'_n(s))^2) ds + \frac{1}{(s_b - s_a)} \int_{s_a}^{s_b} (L_1(s) + \nu L'_1(s))^2 ds, \end{aligned} \quad (39)$$



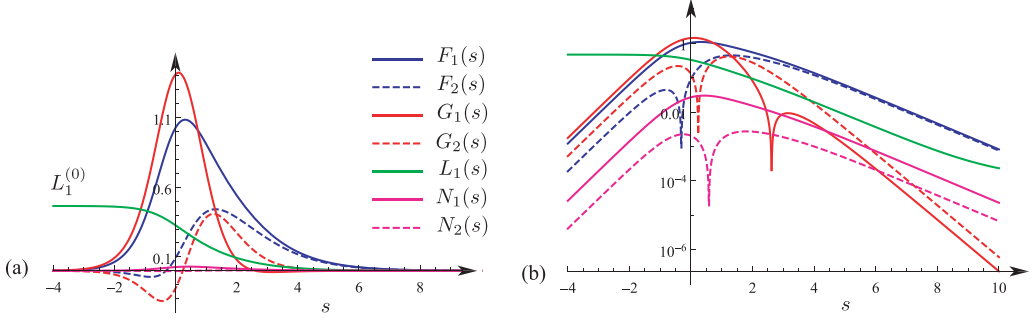


FIG. 2. Numerical simulation for  $N^* = 2$  with  $L_2(s) = 0$  and all other amplitudes different from zero. The parameters are  $\nu = 1.15231$  and  $L_1^{(0)} = 0.465872$  from Table I. Plot (a) is in linear scale, whereas plot (b) is in log-scale of the absolute value of the amplitudes; this plot allows us to distinguish that  $N_1(s)$  is one order of magnitude smaller than  $L_1(s)$ . Moreover,  $N_2(s)$  is another order of magnitude smaller than  $N_1(s)$ . These facts indicate the validity of the Elgindi approximation.

where the interval  $[s_a, s_b] \subset [s_{\min}, s_{\max}]$  is chosen with  $s_a = 10$  and  $s_b = 13 < s_{\max} = 15$ . The error function (39) is iteratively optimized until a condition is reached. Usually this condition concerns an error threshold of  $10^{-7}$ , or a maximum number of iterations. (See Appendix D for more details.)

Figure 2 depicts a standard numerical integration using this algorithm for  $N^* = 2$ . Figure 2(b) in a semilog scale, reveals some interesting features. Particularly, the large  $s$  limit clearly demonstrates that all amplitudes decay as a power law in  $\xi$ . Additionally, in the limit  $s \rightarrow -\infty$ , the  $e^{\sigma s}$  behavior with  $\sigma = 2$  is observed. Finally, both  $N_1(s)$  and  $N_2(s)$  exhibit much smaller absolute values compared to other amplitudes, justifying the Elgindi approximation.

In our earlier work [21], we explored the existence of a finite-time self-similar axisymmetric flow using the Elgindi approximation. This approximation disregards the  $N_n(s)$  functions for  $n \geq 1$  and the functions  $L_n(s)$  for  $n > 1$ . Since, precisely, these functions are responsible for the instability of FP1 (29), we omit them in the subsequent numerical computations. We plan to pursue the full study using a different numerical scheme in a future publication to confirm the current scenario.

The numerical scheme is straightforward for small  $N^*$ , such as 2 or 4. The case  $N^* = 4$  is reported in Fig. 6 in Appendix C. However, in practice, the situation becomes more intricate for  $N^* \gtrsim 8$  (see Fig. 3). This complexity arises because, as  $N^*$  increases, the linear stability of the FP2 allows for a large number of oscillatory unstable modes with a real part greater than  $\sigma$ . Consequently, the trajectory oscillates around the heteroclinic orbit while correctly approaching the large  $s$  asymptotic behavior. As an illustrative example, we present the numerical solution of a heteroclinic orbit in Fig. 3(b). These fast oscillatory modes are also present in the case documented in Ref. [21].

We believe these oscillatory modes to be an artifact of the truncation process, because these are a consequence of the large number of complex eigenvalues obtained from the spectrum of the matrix (37) as  $N^*$  increases. Nevertheless, as  $N^*$  increases, increasingly complex unstable eigenvalues become apparent, resulting in the numerically observed oscillatory behavior. This leads to an increase in the absolute values of the amplitudes  $F_n(s)$  and  $G_n(s)$ , while maintaining bounded the sum:  $\sum_m \beta_{nm} F_m(s)$ , on the right-hand side of the last two equations in Eq. (28). Therefore, we focus our search on the convergent behavior of  $L_1(s)$  and  $N_1(s)$  for various truncations, ultimately obtaining satisfactory convergent results with this criterium.

To extract the accurate profile for the function  $L_1(s)$  and  $N_1(s)$ , we utilize an averaging technique that combines the upper and lower envelopes of the oscillatory solution, defining the resultant functions as  $\bar{L}_1(s)$  and  $\bar{N}_1(s)$  in Fig. 3. Figure 3(a) plots the amplitude  $L_1(s)$ , which is a rapidly oscillating function. We constructed an average function  $\bar{L}_1(s)$  by averaging the upper and lower envelopes of the original oscillating function  $L_1(s)$ . Figure 3(b) illustrates a two dimensional

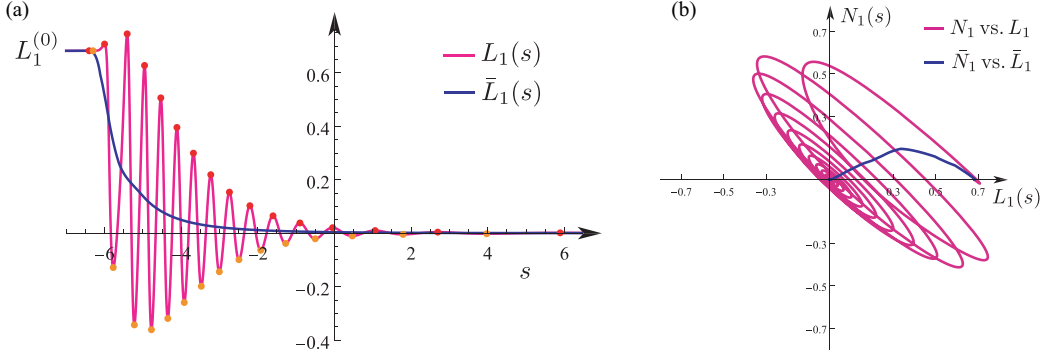


FIG. 3. Numerical simulation for  $N^* = 8$  with the parameters  $\nu = 1.87994$  and  $L_1^{(0)} = 0.682561$ . Adopting the Elgindi approximation, we set  $N_{n>1}(s) = 0$  and  $L_{n>1}(s) = 0$ . (a) The plot shows the relevant amplitude  $L_1(s)$  in magenta. For simplicity, only  $L_1(s)$  is plotted to avoid the complex behavior of the other amplitudes. The amplitude  $L_1(s)$  oscillates quickly around an average function  $\bar{L}_1(s)$  obtained as an iterative average of the envelope functions of the original  $L_1(s)$ . (b) The 2D projection of the heteroclinic orbit displays a fast oscillating behavior near the fixed point FP1 and the heteroclinic trajectory represented by the parametric curve  $\bar{N}_1(s)$  vs  $\bar{L}_1(s)$ .

projection of the heteroclinic orbit for  $N^* = 8$ , depicting this phenomenon. In Appendix C, we provide in detail how this averaging process operates.

The outcome of this process for various values of  $N^*$  is presented in the master curves for  $L_1(s)$  and  $N_1(s)$  in Fig. 4. Numerically and empirically, this approach demonstrates a satisfactory convergence of solutions as  $N^*$  increases, providing compelling evidence for a pointlike finite-time singularity in the solutions of the Euler equations.

Furthermore, the numerical simulations of the heteroclinic orbit yield the value of  $\nu$  for which the solution exists. Figure 5 illustrates the dependence of  $\nu$  as a function of  $1/N^*$  obtained by a linear fit from the data of the Table I in Appendix F:

$$\nu_{N^*} = 2.07774 - 0.318548 \frac{1}{N^*}$$

(red segmented line (4) in Fig. 5). Additionally, applying the Shanks transformation [23] to enhance convergence, the resulting linear fit of the corresponding data of the Table I in F, leads to

$$\nu_{N^*} = 2.0378 + 0.0949636 \frac{1}{N^*},$$

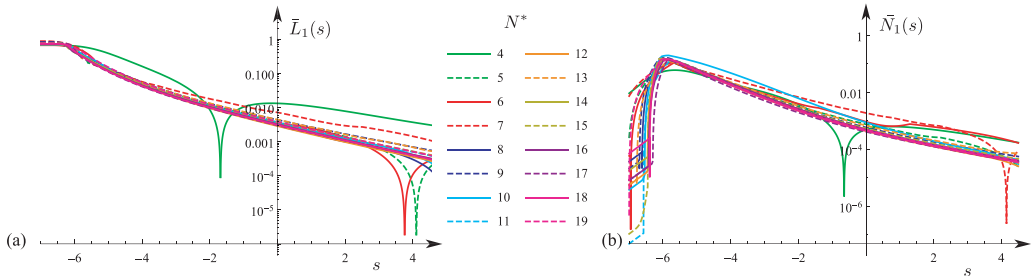


FIG. 4. (a) Once the oscillatory behavior is mitigated, the absolute value of average function  $\bar{L}_1(s)$  is overlaid for varying values of the truncation parameter  $N^*$ , as shown, illustrating favorable convergence. (b) Same plot but for  $\bar{N}_1(s)$ .

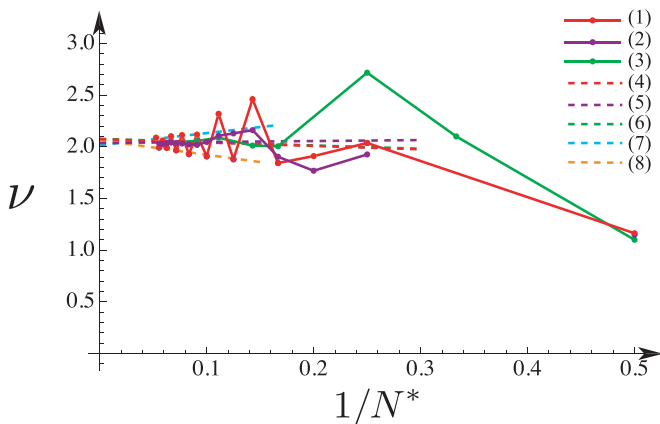


FIG. 5. Plot of the numerically estimated “nonlinear eigenvalue,”  $\nu$ , in relation to the inverse of the truncation parameter  $N^*$ . (1) represents the values by circular red dots joined by lines indicating the numerically estimated data of Table I; (2) represents the same data (in purple) iterated once by the Shanks transformation [23]; (3) plot of the data using a Fourier basis of Table III as in Ref. [21] (in green). The segmented lines represent simple linear fits indicating an estimated convergence of: (4) data using the Legendre basis; (5) data using the Shanks transformation; (6) data using the Fourier basis; (7) data using the odd estimations; (8) data using the even estimations. The complete dataset is compiled in Appendix F.

confirming a similar value,  $\nu \approx 2$  (purple segmented line (5) in Fig. 5). Finally, armed with the knowledge that  $\nu \approx 2$ , we find self-similar solutions using a Fourier basis (see Ref. [21]). These results are summarized in Table III in Appendix F. An identical linear fit to this data yields similar results (green segmented line (6) in Fig. 5):

$$\nu_{N^*} = 2.07549 - 0.330279 \frac{1}{N^*}.$$

Additionally, we present the data for odd  $N^*$ :  $\nu_{N^*} = 2.01646 + 1.17256 \frac{1}{N^*}$  (cyan segmented line (7) in Fig. 5); the data for even  $N^*$ :  $\nu_{N^*} = 2.06544 - 1.41497 \frac{1}{N^*}$  (orange segmented line (8) in Fig. 5).

These fits unveil a convergence rate towards a finite value, approximately  $\nu \rightarrow \nu^* \approx 2.03$  as  $N^* \rightarrow \infty$ . Finally, after obtained the amplitudes solutions at a given order it is possible to reconstruct the whole self-similar structure of the flow. This is shown in Fig. 1.

## VII. DISCUSSION

Assuming that the Euler equations allow for a self-similar finite-time blow-up solution transforms the problem into a search for a heteroclinic orbit within the dynamical system. This orbit connects two distinct fixed points, representing the boundary conditions of the initial problem. The numerical analysis exhibits a consistent convergence pattern in the scheme, resulting in a self-similarity exponent of  $\nu^* \approx 2.03$ . As expected, this differs from the exponent  $\nu_{\text{Luo-Hou}} \approx 2.91$  obtained by Luo and Hou, who studied a singularity emerging on a finite circular rim at the domain’s boundary. We plan to tackle this case using the present method in a future publication.

In a similar context, an intriguing question arises regarding an anularlike singularity of finite radius, say  $R^*$ , in an infinite domain. This assumption of a distance,  $R^*$ , fundamentally alters the original problem [24] and may involve different families of self-similar parameters, potentially transitioning from a dynamical system governed by ordinary differential equations to a nonlinear PDE. How this scenario aligns with the current investigation of a pointlike singularity remains an unresolved issue.

The proximity of the obtained exponent to 2 prompts the conjecture that the true exponent might be precisely  $\nu = 2$ . This conjecture introduces the possibility of exploring solutions to the Euler-Leray equations (6) and (7) for  $\nu = 2$ , simplifying the analytical or numerical task. Assuming, assuming  $\nu = 2$  implies the existence of a crucial parameter with units of acceleration ( $L/T^2$ ), denoted as  $g$ , which establishes the scaling relation  $|\mathbf{x}| \sim g(t_c - t)^2$  and the scaling velocities by  $|\mathbf{v}| \sim g(t_c - t)$ . The parameter  $g$  is expected to explicitly depend on the global properties of the initial flow, specifically the energy (3) and helicity [1] (with units  $\mathcal{E}_0 \sim L^5/T^2$  and  $\mathcal{H}_0 \sim L^4/T^2$  respectively), giving rise to  $g \sim \mathcal{H}_0^4/\mathcal{E}_0^3$ . Accordingly, we conjecture that whereas both the local energy and helicity of the singular solution vanish at the singular time, because of Eq. (9) and footnote [18], the quotient  $\mathcal{H}^4/\mathcal{E}^3$  remains constant. Additionally, an initial helicity distinct from zero may be a necessary condition for a solution of the Euler equation in an infinite domain to manifest a finite-time blow-up.

Last, we emphasize that by taking the curl of the self-similar velocity (4), a self-similar vorticity dependence is obtained, which hypothetically diverges as in Eq. (12). Consequently, the self-similar *ansatz* implies that vorticity scales as  $|\boldsymbol{\omega}| \sim 1/|t_c - t|$ . According to the Beale-Kato-Magda theorem [20], if the solution falls within the basin of attraction of this self-similar solution, then the vorticity must necessarily blow-up in finite time.

### ACKNOWLEDGMENT

This work was supported by Fondecyt (ANID) under Grant No. 1220369.

### APPENDIX A: SOLUTION OF THE EQ. (20)

Inspired by the expansion of the Green functions in spherical coordinates, we solve the Poisson-type equation (20) for the stream function. In spherical coordinates  $(\xi, \theta)$ , the homogeneous part of Eq. (20) is

$$\frac{\partial^2 \varphi}{\partial \xi^2} + \frac{1}{\xi^2} \left( \frac{\partial^2 \varphi}{\partial \theta^2} - \cot \theta \frac{\partial \varphi}{\partial \theta} \right) = 0.$$

Employing separation of variables for the radial and angular parts, respectively,

$$\varphi(\xi, \theta) = R(\xi)y(\theta), \quad (\text{A1})$$

we obtain that

$$y''(\theta) - \cot \theta y'(\theta) = \lambda y(\theta) \quad \text{and} \quad \xi^2 R''(\xi) = -\lambda R(\xi). \quad (\text{A2})$$

The angular part is a Legendre-type differential equation. The boundary conditions (21) and (22):  $y(0) = y(\pi/2) = 0$ , restrict the solution in terms of the associated Legendre polynomials of even index:

$$y_n(\theta) = -c_n \sin \theta P_{2n}^1(\cos \theta), \quad \lambda_n = -2n(2n+1), \quad c_n = \sqrt{\frac{4n+1}{2n(2n+1)}}. \quad (\text{A3})$$

While the solution to the radial part is given by a power-law  $R(\xi) \propto \xi^k$  with  $k = -2n$  or  $k = 2n+1$ . The eigenfunctions (A3) are orthonormal with respect to the inner product constructed from the orthogonality of the associated Legendre polynomials  $P_l^m(\cos \theta)$ . In the case of  $l$  an even number:  $l = 2n$  and  $m = 1$ , this can be restricted to the interval  $\theta \in [0, \pi/2]$ . Therefore, the correct inner product is

$$\langle f(\cdot), g(\cdot) \rangle = \int_0^{\pi/2} \frac{d\theta}{\sin \theta} f(\theta)g(\theta). \quad (\text{A4})$$

Moreover, the set  $\{y_n(\theta)\}$  is orthonormal:  $\langle y_n(\cdot), y_m(\cdot) \rangle = \delta_{nm}$ , since

$$\int_0^{\pi/2} d\theta \sin \theta P_{2n}^1(\cos \theta) P_{2m}^1(\cos \theta) = \frac{2n(2n+1)}{4n+1} \delta_{nm}.$$

Here  $\delta_{nm}$  is the Kronecker  $\delta$  symbol. Furthermore,  $y_n(\theta)$  is the natural angular basis for the stream function  $\Psi(\xi, \theta)$  and  $\Omega_\phi(\xi, \theta)$ , thus for the velocities  $V_\xi$  and  $V_\theta$ , as well as  $V_\phi^2(\xi, \theta)$  can be expanded in it. The negative sign in  $-c_n$  in Eq. (A3) allows us to recover positive solutions in the domain. The axisymmetric stream function and the axial vorticity expand in the basis (A3) as [see Eq. (24) in Sec. IV]:

$$\Psi(\xi, \theta) = \sum_{n=1}^{\infty} \Psi_n(\xi) y_n(\theta), \quad \Omega_\phi(\xi, \theta) = \sum_{n=1}^{\infty} F_n(\xi) y_n(\theta).$$

This expansion [or Eqs. (24)] is substituted into Eq. (20) of the stream function, and the resulting PDE is projected onto the angular basis (A3) using the inner product (A4), yielding

$$-\xi \sum_{m=1}^{\infty} \tilde{\beta}_{nm} F_m(\xi) = \left( \frac{\partial^2}{\partial \xi^2} - \frac{2n(2n+1)}{\xi^2} \right) \Psi_n(\xi), \quad (\text{A5})$$

where the coefficients of the symmetric tensor  $\tilde{\beta}_{nm}$  are given by

$$\tilde{\beta}_{nm} = \langle y_n, \sin \theta y_m \rangle,$$

and the symbol  $\langle \dots \rangle$  represents the inner product (A4). Finally, Eq. (A5) for the radial amplitudes  $\Psi_n$  is solved by convolving the source  $-\xi \sum_{m=1}^{\infty} \tilde{\beta}_{nm} F_m(\xi)$  with the Green's function of the differential operator,  $G(\xi, \xi')$ , which satisfies an equation similar to the radial ODE in Eq. (A2):

$$\left( \frac{\partial^2}{\partial \xi^2} - \frac{2n(2n+1)}{\xi^2} \right) G(\xi, \xi') = \delta(\xi - \xi'). \quad (\text{A6})$$

Here,  $\delta(\cdot)$  is the one-dimensional Dirac- $\delta$  function.

The solution of Eq. (A6) is determined by regions avoiding divergent solutions. For  $\xi \neq \xi'$ , the solution is  $G_{\xi < \xi'}(\xi, \xi') = A_n(\xi') \xi^{2n+1}$ , and for  $\xi \geq \xi'$ , the solution is  $G_{\xi > \xi'}(\xi, \xi') = B_n(\xi') \xi^{-2n}$ . Imposing continuity and the jump of the derivative at  $\xi = \xi'$ :  $G_{\xi < \xi'}(\xi', \xi') = G_{\xi > \xi'}(\xi', \xi')$  and  $G'_{\xi > \xi'}(\xi', \xi') - G'_{\xi < \xi'}(\xi', \xi') = 1$ , these conditions provide the prefactors  $A_n(\xi')$  and  $B_n(\xi')$ , and the final solution of Eq. (A5) is

$$\Psi_n(\xi) = \frac{\tilde{\beta}_{nm}}{4n+1} \left( \int_0^\xi \left( \frac{\xi}{\xi'} \right)^{-2n} F_m(\xi') \xi'^2 d\xi' + \int_\xi^\infty \left( \frac{\xi}{\xi'} \right)^{2n+1} F_m(\xi') \xi'^2 d\xi' \right). \quad (\text{A7})$$

From the exact expression (A7), two types of functions can be identified: external integrals  $L_n(\xi)$  for  $\xi' > \xi$  and internal integrals,  $N_n(\xi)$ , for  $\xi' < \xi$ . Finally, the stream function is expressed through the expansion (26) and the radial functions  $L_n(\xi)$  and  $N_n(\xi)$  are given by equations (27). Notice that the matrix elements  $\beta_{nm}$  are given explicitly by

$$\beta_{nm} = \frac{\tilde{\beta}_{nm}}{4n+1} = \frac{\langle y_n, \sin \theta y_m \rangle}{4n+1}. \quad (\text{A8})$$

In particular, the case of the first amplitude,

$$L_1(\xi) = \sum_{m=1}^{\infty} \beta_{1m} \int_\xi^\infty d\xi' \frac{F_m(\xi')}{\xi'} = \frac{3}{4} \sqrt{\frac{2}{15}} \sum_{m=1}^{\infty} \int_0^\pi d\theta' \sin^2 \theta' \cos \theta' y_m(\theta') \int_\xi^\infty d\xi' \frac{F_m(\xi')}{\xi'}, \quad (\text{A9})$$

corresponds to the Elgindi approximation [14]. In the current and general case (27), the vorticity amplitudes in the Legendre basis,  $F_m$  in Eq. (27), combine with each  $L_n(\xi)$  through the coefficients  $\beta_{nm}$ .

## APPENDIX B: AXISYMMETRIC EULER EQUATIONS IN THE BASIS OF ASSOCIATED LEGENDRE POLYNOMIALS

To find the axisymmetric Euler equations in the new basis, the axial velocity must also be expressed in terms of the angular basis (A3):

$$V_\phi^2(\xi, \theta) = \xi^2 \sum_{n=1}^{\infty} G_n(\xi) y_n(\theta). \quad (\text{B1})$$

With Eq. (26) for the stream function, the radial and azimuthal velocities are calculated using Eq. (17):

$$\begin{aligned} V_\xi &= \frac{1}{\xi^2 \sin \theta} \xi^3 \sum_{n=1}^{\infty} (N_n(\xi) + L_n(\xi)) y'_n(\theta) = \frac{\xi}{\sin \theta} \sum_{n=1}^{\infty} (N_n(\xi) + L_n(\xi)) y'_n(\theta), \\ V_\theta &= -\frac{1}{\xi \sin \theta} \frac{\partial \Psi}{\partial \xi} = -\frac{\xi}{\sin \theta} \sum_{n=1}^{\infty} (-2n N_n(\xi) + (2n+1) L_n(\xi)) y_n(\theta). \end{aligned} \quad (\text{B2})$$

The transport operator in spherical coordinates becomes

$$V_\xi \frac{\partial}{\partial \xi} + \frac{V_\theta}{\xi} \frac{\partial}{\partial \theta} = \sum_n \frac{y'_n(\theta)}{\sin \theta} (N_n(\xi) + L_n(\xi)) \xi \frac{\partial}{\partial \xi} + \sum_n \frac{y_n(\theta)}{\sin \theta} (2n N_n(\xi) - (2n+1) L_n(\xi)) \frac{\partial}{\partial \theta}. \quad (\text{B3})$$

The transport operator (B3) and the velocities (B2) expressed with the functions (27) allow rewriting the vorticity equation (19), as

$$\begin{aligned} & \sum_{p=1}^{\infty} (F_p(\xi) + v \xi F'_p(\xi)) y_p(\theta) \\ & + \sum_{n,p} \left[ \frac{y_n(\theta) y'_p(\theta)}{\sin \theta} (2n N_n(\xi) - (2n+1) L_n(\xi)) + \frac{y'_n(\theta) y_p(\theta)}{\sin \theta} (N_n(\xi) + L_n(\xi)) \xi \frac{d}{d\xi} \right] F_p(\xi) \\ & = \sum_{n,p} \frac{y_p(\theta)}{\sin \theta} [(y'_n(\theta) + 2n \cot \theta y_n(\theta)) N_n(\xi) + (y'_n(\theta) - (2n+1) \cot \theta y_n(\theta)) L_n(\xi)] F_p(\xi) \\ & + \sum_p ((2G_p(\xi) + \xi G'_p(\xi)) \cot \theta y_p(\theta) - y'_p(\theta) G_p(\xi)). \end{aligned} \quad (\text{B4})$$

However, the swirl velocity equation (16) is as follows:

$$\begin{aligned} & \sum_p (2G_p(\xi) + v \xi G'_p(\xi)) y_p(\theta) \\ & + \sum_{n,p} \left[ \frac{y_n(\theta) y'_p(\theta)}{\sin \theta} (2n N_n(\xi) - (2n+1) L_n(\xi)) + \frac{y'_n(\theta) y_p(\theta)}{\sin \theta} (N_n(\xi) + L_n(\xi)) \xi \frac{d}{d\xi} \right] G_p(\xi) \end{aligned}$$

$$= -2 \sum_{n,p} \frac{y_p(\theta)}{\sin \theta} [(2y'_n(\theta) + 2n \cot \theta y_n(\theta))N_n(\xi) + (2y'_n(\theta) - (2n+1) \cot \theta y_n(\theta))L_n(\xi)]G_p. \quad (\text{B5})$$

Note that the operator in the second term of Eqs. (B4) and (B5), the transport operator, remains the same in both equations. To determine the amplitudes  $F_n(\xi)$  and  $G_n(\xi)$ , Eqs. (B4) and (B5) are projected onto the basis (A3) using the inner product (A4),  $\langle y_l | \cdot \rangle$ , and the following set of ODEs is obtained:

$$\begin{aligned} & (v\delta_{lp} + b_{lnp}N_n(s) + b_{lnp}L_n(s))F'_p(s) + (\delta_{lp} + \alpha_{lnp}N_n(s) + a_{lnp}L_n(s))F_p \\ & = (h_{lnp}N_n(s) + e_{lnp}L_n(s))F_p - d_{lp}(2G_p + G'_p(s)) - c_{lp}G_p, \end{aligned} \quad (\text{B6})$$

$$\begin{aligned} & (v\delta_{lp} + b_{lnp}N_n(s) + b_{lnp}L_n(s))G'_p(s) + (2\delta_{lp} + \alpha_{lnp}N_n(s) + a_{lnp}L_n(s))G_p(s) \\ & = -2N_n(s)(h_{lnp} + b_{lnp})G_p - 2L_n(s)(e_{lnp} + b_{lnp})G_p, \end{aligned} \quad (\text{B7})$$

$$N'_n(s) + (2n+3)N_n = \beta_{nm}F_m, \quad (\text{B8})$$

$$L'_n(s) - 2(n-1)L_n = -\beta_{nm}F_m. \quad (\text{B9})$$

Here, as before, we use the Einstein sum convention when indices are repeated. The equations (B6), (B7), (B8), and (B9) form an infinite hierarchy of ODEs. The coefficients have unique values because the angular basis  $y_n(\theta)$  is fixed, and they are

$$\begin{aligned} b_{lnp} &= \left\langle y_l, \frac{1}{\sin \theta} y'_n y_p \right\rangle, \quad \alpha_{lnp} = 2nb_{lpn}, \quad a_{lnp} = -(2n+1)b_{lpn}, \\ k_{lnp} &= \left\langle y_l, \frac{\cos \theta}{\sin^2 \theta} y_n y_p \right\rangle, \quad h_{lnp} = b_{lnp} + 2nk_{lpn}, \quad e_{lnp} = b_{lnp} - (2n+1)k_{lpn}, \\ c_{lp} &= \langle y_l, y'_p \rangle, \quad d_{lp} = -\left\langle y_l, \frac{\cos \theta}{\sin \theta} y_p \right\rangle, \quad \beta_{nm} = \frac{\langle y_n, \sin \theta y_m \rangle}{4n+1}. \end{aligned} \quad (\text{B10})$$

Contrary to Ref. [21], some tensors are of rank 3 because the swirl velocity and vorticity amplitudes must couple with an infinite array of functions  $N_n(s)$  and  $L_n(s)$  instead of just one function  $L_1(s)$ , as is the case of the approximation in Ref. [21]. The tensors  $b$ ,  $e$ , and  $h$  are symmetric with respect to the first and third indices, while  $k$  and  $d$  are completely symmetric. However,  $\alpha$ ,  $a$ , and  $c$  do not have any symmetry.

The dynamical system (B6)–(B9) can be rewritten in the usual way, as in dynamical system (28).

## APPENDIX C: NUMERICAL SIMULATIONS

For practical purposes, an additional parameter is included to measure the amplitude,  $\gamma$ , of the eigenvector  $\delta \bar{g}$  of the matrix (37). Although this is not relevant because two distinct amplitudes are related by a simple translation in the  $s$  coordinate, it is relevant that the objective domain from the asymptotics remains in the domain of integration, something done by adjusting  $\gamma \delta \bar{g}$ . As already said in Sec. VI, we reproduce here in Fig. 6 the numerical solutions for the case  $N^* = 4$ .

As explained in the main text, as  $N^*$  increases, the linear stability of the fixed point FP2 becomes more complex because oscillatory modes appear, rendering the fixed point FP1 oscillatory and damped around it.

The procedure for generating the average function  $\bar{L}_1(s)$  (or  $\bar{N}_1(s)$ ) is as follows: The points of maxima and minima of  $L_1(s)$  (or  $N_1(s)$ ) are used to interpolate iteratively the upper and lower envelope after calculating their average sets to the left and right. Then, for the two average sets, another pair of averages is calculated, and this process is repeated until a pair of average sets



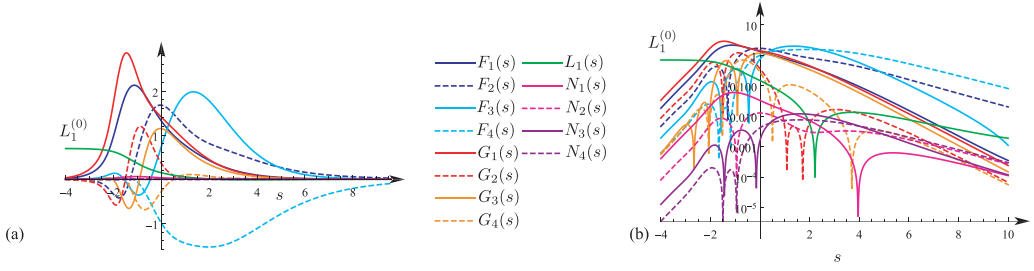


FIG. 6. Numerical simulation for  $N^* = 4$  with  $L_2(s) = L_3(s) = L_4(s) = 0$  and all other amplitudes different from zero. The parameters are  $\nu = 2.03805$  and  $L_1^{(0)} = 0.697295$ . (a) Linear plot for all amplitudes as a function of the  $s$  variable. (b) The log-scale of the absolute value of the amplitudes allows us to distinguish that  $N_1(s)$ ,  $N_2(s)$ ,  $N_3(s)$ , and  $N_4(s)$  are up to four orders of magnitude smaller than  $L_1(s)$ .

is obtained such that both can form a sufficiently smooth quadratic fit. Generally, around four averaging steps are required to obtain a suitable fitted curve. In Figure 7 we show the obtained convergent patterns for average functions  $\bar{L}_1(s)$  and  $\bar{N}_1(s)$  in linear scale.

Figure 3 displays the numerical curve  $L_1(s)$  from  $N^* = 8$ , emphasizing its extreme points, along with  $\bar{L}_1(s)$  corresponding to the quadratic fit of the multiple averages of the extreme points. Similar average procedures are done in Figs. 4 and 7, for the  $\bar{L}_1(s)$  and  $\bar{N}_1(s)$  functions.

#### APPENDIX D: DIFFERENTIAL EVOLUTION ALGORITHM

In what follows, we briefly discuss the differential evolution (DE) algorithm [22] in the context of finding solutions to the eigenvalue problem (28). The set of ODEs composing such a dynamical system, (B6)–(B9), must be solved from a starting point, the fixed point (30), and ending at the fixed point (29). The solution is found by adjusting two parameters: the main one,  $\nu$ , which determines the behavior (31) and a secondary one, the parameter  $\gamma$ , that multiplies all amplitudes in Eq. (32) as  $s \rightarrow -\infty$ . The differential evolution algorithm finds the values of  $(\nu, \gamma)$  that best solve the dynamical system with the fixed points through an iterative minimization process, repeated over  $K_{\max}$  iterations, named generations by the creators of the scheme [22]. We note that DE can easily be applied to find an arbitrary number of parameters, as we did in our early attempt using the Fourier basis [21]. The algorithm is summarized by the following stages:

(1) Initialization: A range of values is set for each parameter,  $\nu_{\text{lower}} \leq \nu \leq \nu_{\text{upper}}$  and  $\gamma_{\text{lower}} \leq \gamma \leq \gamma_{\text{upper}}$ . For instance, we used  $2 - \Delta\nu \leq \nu \leq 2 + \Delta\nu$  with  $|\Delta\nu| < 1$ , and  $1 - \Delta\gamma \leq \gamma \leq 1 + \Delta\gamma$  with  $|\Delta\gamma| < 5$ .

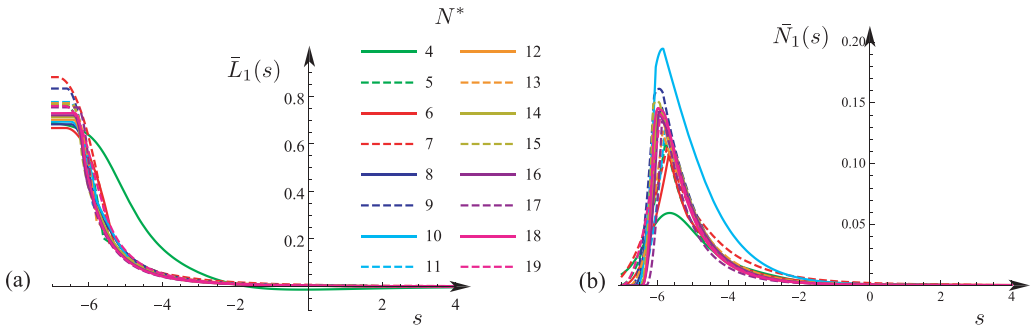


FIG. 7. (a) The average function  $\bar{L}_1(s)$  and (b) the average function  $\bar{N}_1(s)$  are overlaid for varying values of the truncation parameter  $N^*$ , as shown, illustrating favorable convergence.

Then, a number of NP parent tuples  $(v, \gamma)$  are randomly selected with the initial parameter values randomly distributed within the previously defined intervals. This set of parameters forms the seed of what we call the first generation, labeled with the generation index ( $K = 1$ ).

$$\{(v, \gamma)_1^{(K=1)}, \dots, (v, \gamma)_{\text{NP}}^{(K=1)}\}. \quad (\text{D1})$$

After the seed set is determined, the algorithm proceeds with a three stages cycle.

(2) Mutation: Starting from the original seed set, a second set of mutated tuples is generated by sweeping the parameter space with linear combinations of the parent tuples according to the following rule:

$$(v, \rho)_i^{(K+1)} = (v, \gamma)_{r_1}^{(K)} + F((v, \gamma)_{r_2}^{(K)} - (v, \gamma)_{r_3}^{(K)}), \quad i = 1, \dots, \text{NP}. \quad (\text{D2})$$

The three integer indices  $r_1, r_2, r_3$  take specific values for each  $i$ th mutated tuple, and they are chosen randomly from the integer set  $\{1, \dots, \text{NP}\}$ , with the conditions that all  $r_1, r_2, r_3$  are different themselves, and  $r_k \neq i$ . The constant  $F \in [0, 2]$  controls the dispersion of the evolution in the parameters space. We set  $F = 0.5$  for all simulations.

(3) Crossover: Next, a set of successor tuples is generated from the parent tuples (D1) and the mutated tuples (D2). This occurs according to a crossover rate,  $\text{CR} \in [0, 1]$ , which controls the diversity of the evolution:

$$\begin{aligned} V_i^{(K+1)} &= \begin{cases} v_i^{(K+1)} & \text{with probability CR} \\ v_i^{(K)} & \text{otherwise} \end{cases}, \\ \Gamma_i^{(K+1)} &= \begin{cases} \rho_i^{(K+1)} & \text{with probability CR} \\ \gamma_i^{(K)} & \text{otherwise} \end{cases}, \quad i = 1, \dots, \text{NP}. \end{aligned} \quad (\text{D3})$$

For all simulations, we used  $\text{CR} = 0.85$ , which favors diversity.

(4) Selection: From the set of parent and successor tuples, it is selected those that will conform the next generation of parameters by means of a minimization of the error function  $\text{Error}[(v, \gamma)_i^{(K)}]$  defined by Eq. (39):

$$(v, \gamma)_i^{(K+1)} = \begin{cases} (V, \Gamma)_i^{(K+1)} & \text{Error}[(V, \Gamma)_i^{(K+1)}] \leq \text{Error}[(v, \gamma)_i^{(K)}] \\ (v, \gamma)_i^{(K)} & \text{otherwise} \end{cases}, \quad i = 1, \dots, \text{NP}. \quad (\text{D4})$$

The error (39) is computed after solving numerically forward the ODEs (B6)–(B9) with a given truncature  $N^*$  in the domain  $s \in [s_{\min}, s_{\max}]$ , with the initial boundary condition at  $s = s_{\min}$  given by Eqs. (32)–(36), determined by a fixed power  $\sigma \in \mathbb{Z}^+$ . The result of the numerical integration are the functions of amplitudes  $F_n(s)$ ,  $G_n(s)$ ,  $L_1(s)$ , and  $N_n(s)$ ,  $n = 1, \dots, N^*$ , related to both the parent tuple  $(v, \gamma)_i^{(K)}$  or successor tuple  $(V, \Gamma)_i^{(K+1)}$ . At the end of the selection process (D4) the next generation is obtained:

$$\{(v, \gamma)_1^{(K+1)}, \dots, (v, \gamma)_{\text{NP}}^{(K+1)}\}.$$

This evolutionary cycle continues by repeating the stages of: 2. Mutation (D2), 3. Crossover (D3), and 4. Selection (D4). As a general rule, the successor generation of the parameters  $\{(v, \gamma)_i^{(K+1)}\}$  will have a lower error than the previous generation  $\{(v, \gamma)_i^{(K)}\}$ . This cycle is repeated until reaching an error lower than a threshold  $\text{Error}_{\min}$  or after reaching a maximum generation  $K_{\max}$  steps. For all simulations, we used  $\text{Error}_{\min} = 10^{-7}$ , whereas  $K_{\max}$  is varied in the range  $\in [10, 100]$ . If the evolution finishes in the last generation  $K_{\max}$  without crossing the threshold, or if more than one tuple crossed it, one selects the tuple with the lowest error. Finally, if this error does not meet expectations, that is, to be at least lower than  $10^{-3}$ , the tuple  $(\bar{v}, \bar{\gamma})^{(K=K_{\max})}$  is used as a reference point to build a new range of parameters, and Differential Evolution is applied again.

## APPENDIX E: THE SHANKS TRANSFORMATION

The Shanks transformation is defined as [23]

$$S(\nu_{N^*}) = \frac{\nu_{N^*+1}\nu_{N^*-1} - (\nu_{N^*})^2}{\nu_{N^*+1} + \nu_{N^*-1} - 2\nu_{N^*}}.$$

Applying  $S(\cdot)$  successively to the sequence of  $\nu_{N^*}$  results in an improvement sequence as it may be seen in the Table I.

APPENDIX F: TABLES WITH THE CONVERGENCE SEQUENCES  
OF  $\nu$  FOR VARIOUS NUMBER OF MODES

TABLE I. Summary of the numerical solutions to Eq. (28) with  $L_1(s) \neq 0$  and at least  $N_1(s) \neq 0$  for  $\sigma = 2$ . The table compiles the values of  $\nu_{N^*}$ , the improvement convergence  $S(\nu_{N^*})$ , the amplitude  $L^{(0)}(\sigma, \nu_{N^*})$ , the  $\text{Error}(\nu_{N^*}, \gamma)$  (calculated between  $s_a = 10$  and  $s_b = 13$ ), the parameter  $\gamma$ , and the starting point of the integration interval  $s_{\min}$ . For all simulations,  $s_{\max} = 15$ .

$N^*$	$\sigma$	# Nodes	$\nu_{N^*}$	$S(\nu_{N^*})$	$L^{(0)}(\sigma, \nu_{N^*})$	$\text{Error}(\nu_{N^*}, \gamma)$	$\gamma$	$s_{\min}$
2	2	0	1.15231	—	0.465872	$8.77849 \times 10^{-8}$	-1.55707	-4.0
3	2	—	—	—	—	—	—	—
4	2	1	2.03805	—	0.697295	$1.3851 \times 10^{-6}$	-1.62375	-4.0
5	2	17	1.91086	1.76923	0.763168	$5.98668 \times 10^{-7}$	0.098675	-7.0
6	2	12	1.84385	1.90431	0.666764	$9.38614 \times 10^{-6}$	3.05798	-7.0
7	2	14	2.46257	2.1625	0.88108	$1.04847 \times 10^{-3}$	3.77645	-7.0
8	2	29	1.87994	2.13078	0.682561	$1.66852 \times 10^{-6}$	3.85702	-7.0
9	2	44	2.32043	2.10764	0.833166	$1.18286 \times 10^{-5}$	1.20205	-7.0
10	2	44	1.90880	2.04785	0.693843	$2.47026 \times 10^{-4}$	4.20024	-7.0
11	2	44	2.11878	2.01946	0.776424	$9.76532 \times 10^{-7}$	3.51113	-7.0
12	2	51	1.9303	2.02344	0.70191	$1.79167 \times 10^{-5}$	2.12087	-7.0
13	2	27	2.11442	2.03276	0.771508	$8.88566 \times 10^{-5}$	3.95846	-7.0
14	2	53	1.96769	2.03814	0.712948	$2.03255 \times 10^{-4}$	3.37468	-7.0
15	2	53	2.10321	2.04262	0.766154	$2.26803 \times 10^{-6}$	3.29063	-7.0
16	2	69	1.99363	2.0357	0.720714	$1.54934 \times 10^{-4}$	2.86086	-4.0
17	2	94	2.06191	2.02777	0.754146	$1.3032 \times 10^{-4}$	3.23987	-7.0
18	2	128	2.02397	2.03353	0.729197	$1.64111 \times 10^{-2}$	2.74248	-7.0
19	2	98	2.08961	—	0.759612	$1.7957 \times 10^{-5}$	2.82809	-7.0

TABLE II. Summary of the numerical solutions to Eq. (28) for various  $\sigma \neq 2$  with  $L_1(s) \neq 0$  and all  $N_{n \leq N^*}(s) \neq 0$  if  $N^* \leq 3$ , or just  $L_1(s)$  and  $N_1(s) \neq 0$  if  $N^* > 3$ . The table compiles the values of  $\sigma$ ,  $\nu_{N^*}$ , the amplitude  $L^{(0)}(\sigma, \nu_{N^*})$ , the  $\text{Error}(\nu_{N^*}, \gamma)$  which is calculated between  $s_a = 10$  and  $s_b = 13$ , the parameter  $\gamma$ , and the starting point of the integration interval  $s_{\min}$ . For all simulations,  $s_{\max} = 15$ .

$N^*$	$\sigma$	# Nodes	$\nu_{N^*}$	$L^{(0)}(\sigma, \nu_{N^*})$	$\text{Error}(\nu_{N^*}, \gamma)$	$\gamma$	$s_{\min}$
1	1	0	1.0874	0.56368	$3.09913 \times 10^{-9}$	2.10499	-4.0
1	3	2	0.921274	1.21765	$8.41735 \times 10^{-5}$	6.86957	-7.0
2	3	0	0.81556	0.405925	$1.92999 \times 10^{-7}$	-4.53568	-4.0
2	4	0	0.684418	0.384183	$1.12285 \times 10^{-5}$	-1.13553	-4.0
3	4	1	1.6314	0.611404	$2.12396 \times 10^{-6}$	3.70325	-7.0
3	5	2	1.20285	0.487731	$1.74334 \times 10^{-5}$	3.31115	-4.0
5	3	9	1.77806	0.669516	$1.94065 \times 10^{-6}$	2.07253	-7.0
5	4	39	2.15347	0.772235	$1.76294 \times 10^{-3}$	2.98594	-6.0
6	3	13	1.81132	0.678624	$6.38356 \times 10^{-6}$	3.09318	-7.0
6	4	13	1.71446	0.648294	$5.06123 \times 10^{-6}$	2.21908	-7.0
7	3	20	1.68884	0.645082	$7.91539 \times 10^{-6}$	5.71461	-7.0
7	4	12	1.90463	0.701519	$8.43189 \times 10^{-6}$	3.75825	-6.0
9	3	32	1.87938	0.697264	$7.53346 \times 10^{-6}$	4.82398	-7.0
9	4	56	2.02616	0.737502	$4.37623 \times 10^{-5}$	3.80158	-6.0
10	3	32	1.94604	0.715518	$3.12218 \times 10^{-5}$	3.76612	-7.0
10	4	40	1.86536	0.691259	$1.85541 \times 10^{-5}$	6.11158	-6.0

TABLE III. Numerical solutions to dynamical system (28) with a Fourier angular base and Elgindi approximation, only  $L_1(s) \neq 0$  and all  $N_n(s) = 0$ , for  $\sigma = 2$ . Here  $s_{\max} = 30$  while the error interval is between  $s_a = 26$  and  $s_b = 29$ . Solutions from  $N^* = 2$  to  $N^* = 4$  were presented in Ref. [21].

$N^*$	$\sigma$	# Nodes	$\nu_{N^*}$	$L^{(0)}(\sigma, \nu_{N^*})$	$\text{Error}(\nu_{N^*}, \gamma)$	$\gamma$	$s_{\min}$
2	2	0	1.10091	1.40061	$3.10847 \times 10^{-7}$	-1.14264	-7.0
2	2	1	1.31387	1.54258	$4.76247 \times 10^{-5}$	-1.0	-7.0
3	2	2	2.10121	2.06747	$8.60559 \times 10^{-2}$	-0.720427	-13.2
4	2	2	2.7186	2.47909	$3.28488 \times 10^{-1}$	-1.0	-10.0
6	2	1	2.00607	2.00405	$1.29802 \times 10^{-1}$	-1.28305	-7.0
7	2	8	2.01267	2.00845	$5.74778 \times 10^{-2}$	-1.40662	-7.0
9	2	56	2.08925	2.0595	$2.61271 \times 10^{-3}$	-0.717312	-5.0
11	2	30	2.05733	2.03822	$4.12929 \times 10^{-3}$	-1.64337	-7.0
15	2	2	2.04474	2.02983	$6.04261 \times 10^{-2}$	-1.2498	-7.0
16	2	169	2.03126	2.02084	$1.1883 \times 10^{-3}$	-1.86289	-7.0

- [1] In addition to the energy, linear momentum, and others, the Euler equations posses another global conserved quantity, the helicity [25,26]:

$$\mathcal{H} = \int \mathbf{v}(\mathbf{x}, t) \cdot \boldsymbol{\omega}(\mathbf{x}, t) d\mathbf{x}.$$

- [2] L. Euler, Principes généraux du mouvement des fluides, Mem. Acad. Sci. Berlin **11**, 274 (1757).  
 [3] L. Lichtenstein, Über einige Existenzprobleme der Hydrodynamik, Math. Z. Phys. **23**, 89 (1925).  
 [4] N. Gunther, On the motion of fluid in a moving container, Izvestia Akad. Nauk USSR, Ser. Fiz. Mat. **20**, 1323 (1927).  
 [5] G. Luo and T. Y. Hou, Potentially singular solutions of the 3D axisymmetric Euler equations, *Proc. Natl. Acad. Sci. USA* **111**, 12968 (2014).  
 [6] Y. Wang, C.-Y. Lai, J. Gómez-Serrano, and T. Buckmaster, Asymptotic self-similar blow-up profile for three-dimensional axisymmetric euler equations using neural networks, *Phys. Rev. Lett.* **130**, 244002 (2023).  
 [7] Jiajie Chen and Thomas Y. Hou, Stable nearly self-similar blowup of the 2D Boussinesq and 3D Euler equations with smooth data, [arXiv:2210.07191](https://arxiv.org/abs/2210.07191).  
 [8] Y. Pomeau, Singularité dans l'évolution du fluide parfait, C. R. Acad. Sci. Paris **321**, 407 (1995).  
 [9] Y. Pomeau, On the self-similar solution to the Euler equations for an incompressible fluid in three dimensions, *C. R. Mec.* **346**, 184 (2018).  
 [10] Y. Pomeau, M. Le Berre, and T. Lehner, A case of strong non linearity: Intermittency in highly turbulent flows, *C. R. Mec.* **347**, 342 (2019).  
 [11] Y. Pomeau and M. Le Berre, Blowing-up solutions of the axisymmetric Euler equations for an incompressible fluid, [arXiv:1901.09426](https://arxiv.org/abs/1901.09426).  
 [12] C. Josserand, Y. Pomeau, and S. Rica, Finite-time localized singularities as a mechanism for turbulent dissipation, *Phys. Rev. Fluids* **5**, 054607 (2020).  
 [13] Juliette Amauger, Christophe Josserand, Yves Pomeau, and Sergio Rica, Two dimensional singularity turbulence, *Physica D* **443**, 133532 (2023).  
 [14] T. M. Elgindi, Finite-time singularity formation for  $C^{1,\alpha}$  solutions to the incompressible Euler equations on  $\mathbb{R}^3$ , *Ann. Math.* **194**, 647 (2021).  
 [15] J. Eggers and M. A. Fontelos, *Singularities: Formation, Structure, and Propagation*, Cambridge Texts in Applied Mathematics (Cambridge University Press, Cambridge, UK, 2015).  
 [16] J. Leray, Sur le mouvement d'un liquide visqueux emplissant l'espace, *Acta Math.* **63**, 193 (1934).  
 [17] The stability of the obtained solutions respect to a similarity time  $\tau = -\log(t_c - t)$  will be studied in a future publication.  
 [18] As the energy, the helicity of a pointlike singularity must not diverge as  $t \rightarrow t_c$ , thus

$$\begin{aligned} \mathcal{H} &= \int \mathbf{v}(\mathbf{x}, t) \cdot \boldsymbol{\omega}(\mathbf{x}, t) d\mathbf{x} = \frac{1}{(t_c - t)^{2-\nu}} \int \mathbf{V}\left(\frac{\mathbf{x}}{(t_c - t)^\nu}\right) \cdot \boldsymbol{\Omega}\left(\frac{\mathbf{x}}{(t_c - t)^\nu}\right) d^3\mathbf{x} \\ &= (t_c - t)^{4\nu-2} \int \mathbf{V}(\boldsymbol{\xi}) \cdot \boldsymbol{\Omega}(\boldsymbol{\xi}) d^3\boldsymbol{\xi}, \end{aligned}$$

hence:  $\nu \geq 1/2$ , which includes the energy condition after Eq. (9) if  $\int \mathbf{V}(\boldsymbol{\xi}) \cdot \boldsymbol{\Omega}(\boldsymbol{\xi}) d^3\boldsymbol{\xi} \neq 0$ . Therefore, one concludes that for consistency  $\nu \geq 1/2$ , as it is obtained.

- [19] M. Schonbek, Nonexistence of pseudo-self-similar solutions to incompressible Euler equations, *Acta Math. Sci.* **31**, 2305 (2011).  
 [20] J. T. Beale, T. Kato, and A. Majda, Remarks on the breakdown of smooth solutions for the 3-D Euler equations, *Commun. Math. Phys.* **94**, 61 (1984).  
 [21] R. Cádiz, D. Martínez-Argüello, and S. Rica, Axisymmetric self-similar finite-time singularity solution of the euler equations, *Adv. Contin. Discrete Models* **2023**, 30 (2023).  
 [22] Rainer Storn and Kenneth Price, Differential evolution—A simple and efficient heuristic for global optimization over continuous spaces, *J. Global Optim.* **11**, 341 (1997).  
 [23] C. M. Bender and S. A. Orszag, *Advanced Mathematical Methods for Scientists and Engineers* (McGraw-Hill, New York, NY, 1978).

- [24] Sergio Rica, Potential anisotropic finite-time singularity in the three-dimensional axisymmetric Euler equations, [Phys. Rev. Fluids](#) **7**, 034401 (2022).
- [25] J-J. Moreau, Constantes d'un îlot tourbillonnaire en fluide parfait barotrope [constants of an island of turbulence in a perfect barotropic fluid], C. R. Hebd. Seances Acad. Sci., Paris **252**, 2810 (1961).
- [26] H. K. Moffatt, The degree of knottedness of tangled vortex lines, [J. Fluid Mech.](#) **35**, 117 (1969).